To the Oklahoma State University:

The members of the Committee approve the honors thesis of Zach DeGeorge completed on December 3, 2021

Andrew J. Yost, Chairperson

Mario F. Borunda, Committee Member

DeGeorge, Zach; *Mo-Mo dimer doped ZnS quantum dots and their influence on Hybrid Halide Perovskite Heterostructure Solar Cells*

Abstract: Quantum dots are semiconducting particles on the nanometer scale which exhibit unique size dependent electronic and optical properties due to the quantum confinement phenomenon. Over the past several years colloidal quantum dots have been garnering more attention with their rise in photovoltaic device performance and power efficiency, from 3.5% in 2010 to 16.6% in 2019. Many of the attempts to improve photovoltaics' overall device efficiency have been focused on device architecture and materials improvement. Doping chalcogenide-based quantum dots with transition metals like Mn or Co has been shown to dramatically improve device efficiency and overall light absorption, respectively. In this research project, Mo-Mo-dimers (Mo_d) are doped into ZnS quantum dots using a wet chemical method. The quantum dot's optical properties, crystallinity, and size are explored using optical absorption spectroscopy, X-ray diffraction, and transmission electron microscopy. Then the quantum dots are incorporated, via successive ionic layer adsorption and reaction, into a solar cell architecture to form a p-n junction with a hybrid halide perovskite film. The hybrid halide films in this project consist of $CH_3NH_3PbI_3$ due to their reported high efficiencies in photovoltaic cells. The overall goal is to observe and interpret changes in the open-circuit voltage and short-circuit current of a working photovoltaic cell in order to determine if Mo_d doping has any efficacy when combined with hybrid halide perovskite films.

Mo-Mo dimer doped ZnS quantum dots and their influence on Hybrid Halide Perovskite Heterostructure Solar Cells

By

Zach DeGeorge

An honors thesis submitted to the Department of Physics and the Oklahoma State University in partial fulfillment of the requirements for the degree of

Bachelor of Science

in

Applied Physics

Stillwater, Oklahoma

December 3, 2021

COPYRIGHT PAGE

Acknowledgments

I would like to extend thanks to Trieu Le, Thilini Ekanayaka, Halle Hellfrich, Dr. Elena Echeverria, Dr. Shoukath Sulthana, Dr. Yolanda Vasquez, Dr. Mario Borunda, and Dr. Andrew Yost for their contributions to this thesis. I would also like to thank Oklahoma State University for their support of research activity through startup funding and the OSU Physics Department for providing resources to allow for the completion of this thesis.

Table of Contents

List of Figures and Tables

Chapter One

Introduction

Ever since the late nineteenth century, mankind has become aware of an alarming trend; the slow increase of temperatures across the planet and gradual shifts in climate patterns known as global warming and climate change respectively. The need to address this trend has slowly advanced to the forefront of scientific study, including one-half of the 2021 Nobel Prize in Physics being awarded to research regarding climate modeling. According to an Intergovernmental Panel on Climate Change report published in 2018, (1) the Global Mean Surface Temperature (GMST) has risen by just over 1 °C since pre-industrial levels taken in 1860, with nearly 100% of this change being attributed to what the committee defines as Human-Induced Temperature Change. The committee determines that while anthropogenic emissions (greenhouse gases, aerosols, and their precursors) up to the present are unlikely to result in more than 0.5 °C warming over the next century, they also state that reaching and sustaining net zero global anthropogenic CO_2 emissions and declining net non-CO_2 radiative forcing would effectively halt anthropogenic global warming on a multi-decade scale. A separate study (2) focused on using a multi-method reconstruction approach to analyze Holocene GMST dating back 12,000 years highlights the dangerously rapid rise in global warming in the past 150 years and its inconsistency with historical cycles of planetary warming and cooling. While there are few who would openly deny the existence of such trends, the main challenge for modern society is adequately addressing such issues while accounting for economic and quality of life factors.

A report published in the U.S. Energy Information Administration (3) in 2016 found that countries not participating in Organization for Economic Cooperation and Development (non-OECD) would increase their CO_2 emissions the most by 2050, specifically China and India, figure 1. A significant reason for the continued dependence on fossil fuels is the lack of viable renewable alternatives that are both efficient enough to meet the large-scale energy demands of countries and are economically feasible in both developing and developed nations. While solar cells have a clear environmental advantage over fossil fuels, even the best commercially available (non-research grade) photovoltaics range from 15-22% (4) efficient while the combined heat and power (CHP) systems using natural gas are up to 80% (5) efficient and are the most energy-efficient method of generating power today. In addition to these concerns, renewables such as solar have high start-up costs and lack the ability to store large quantities of energy in the same way traditional fossil fuels do. While these realities do present several challenges for the global renewable transition, laboratory data on solar cells has shown promise and some cells have shown theoretical efficiencies of up to 66%. One area of solar cell development that has shown to be potentially promising is hybrid halide perovskite (HHP) based solar cells.

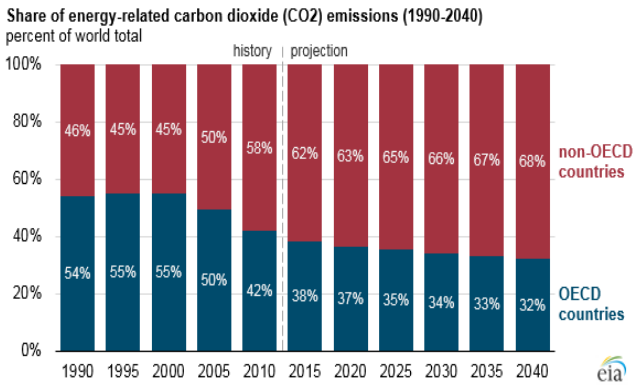

Figure 1: *Global CO_2 emission shares comparison between OECD and non-OECD participating countries from 1990-2040 adapted from (3)*

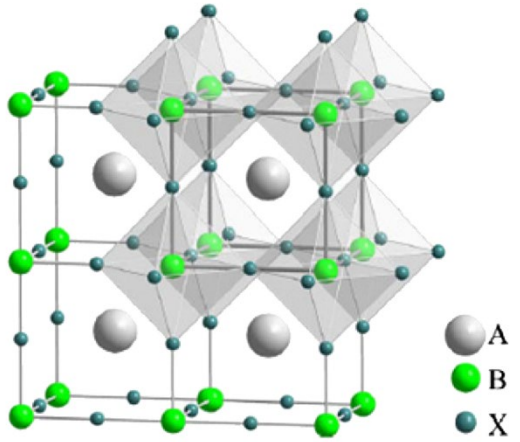

Figure 2: Ball and stick model of perovskite crystal structure adapted from (6)

A perovskite is a material that follows the chemical formula ABX_3 where A and B represent cations in the structure and X represents an anion that binds the two cations together, figure 2. The first mention of perovskite materials was in 1893 in the article, "*Über Die Casium- Und Kalium-Bleihalogenide",* reports on the perovskite CaTiO3. (7) There is an extensive history of research related to perovskites which are beyond the scope of this thesis but interested readers should refer to the following literature references (8, 9). The complex nature of the perovskite structure would lead one to think that a large number of different elements could be combined to form perovskite compounds. In fact, the perovskite structure, specifically stable instances of ABX_3, are governed by the Goldschmidt (9) equation:

$$T_F = \frac{(R_A + R_X)}{\sqrt{2}(R_B + R_X)} \quad (1)$$

where R_A, R_B and R_X are the ionic radii of A, B and X, respectively. A narrow range of elements can satisfy this guiding principle, but in-theory and in-practice the relative positions of the A,B, and X atoms can be manipulated via strain engineering and different growth methods which, in turn, allows perovskites to possess a wide array of chemical, electrical, and optical properties. In this project the type of ABX_3 perovskite is known as a hybrid halide perovskite (7). The A site contains $CH_3NH_3^+$, the B site contains Pb^{2+}, and the X site contains I^- is written as $CH_3NH_3PbI_3$.

Over the past decade, many efforts have been devoted to researching these HHP materials across the world. In 2012, researchers first discovered how to make a stable, thin-film perovskite solar cell using lead halide perovskites with a photon-to-electron conversion efficiency of over 10% (10). This showed the potential that these materials had to change the future of solar cell technology. Currently, the highest performing all perovskite cell has a stabilized efficiency of 25.6% with a 0.0804 cm^2 active area (11), whereas the highest performing HHP-Si tandem cells have device efficiencies of 25.6% with active area of 0.049 cm^2 and 24.2% with active area of 1 cm^2 (12) and recently in 2021 reached 29.8% efficiency (13). Much of the current research reflects that the highest performing HHP based solar cells incorporate the perovskites into heterojunctions. These heterojunctions are typically p-n, p-i-n, or some type of tandem multi-layered heterostructure due to the desired high performance of these type of structures (14). Relatively little emphasis has been given to incorporating different nanostructures, such as dilute magnetic semiconducting quantum dots, into these layered heterostructures as a path toward improved device/material performance.

Quantum dots are semiconductor nanocrystals that exhibit size-dependent optical and electrical properties. These size dependent properties allow for easy bandgap and band structure engineering which can lead to boosts in energy conversion efficiency of the device (15). The size dependent phenomenon is known as 'Quantum confinement' and describes the confinement of the electron wave function to the physical dimensions of the particles resulting in the spatial confinement of electron-hole pairs, also known as excitons, in one or more dimensions within a material and the electronic energy levels become discretized (16). Although size changes are subtle the optical and electronic band structure can change dramatically. One way to improve device efficiency is to enhance the conduction band and valence band offset by changing the bandgap. This can be done in a variety of ways, mostly through growth parameters or device architecture. In quantum dots for example, as the size of the particle decreases, the band gap increases, figure 3, this may introduce previously forbidden optical/electronic transition on the other hand it may allow for less favorable absorption if the band gap increases too much. While the size of the quantum dots is an important area in the study of photovoltaics, another equally important area of focus is that of the composition of the quantum dots.

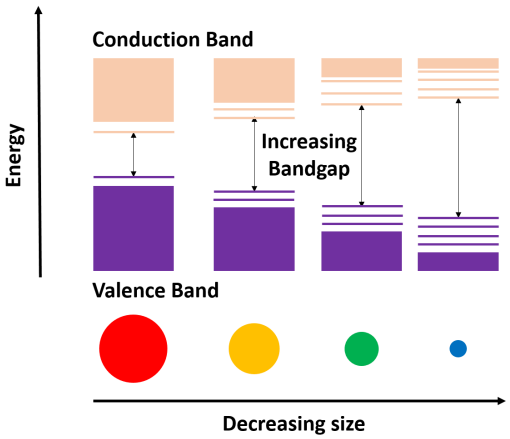

Figure 3: *Schematic of particle size vs bandgap under quantum confinement phenomenon. Conduction band is pink and valence band is purple the lines indicate the discrete states.*

Introducing dopants will shift and mold the band structure and possibly result in different stoichiometry and crystal structure which is favorable in different environments. Dilute magnetic semiconductor (DMS) quantum dots are semiconducting quantum dots that exhibit magnetic properties due to a low concentration of magnetic dopants or vacancy defects. The doping concentration range varies but typically does not exceed 10% of the total material as this concentration borders on the formation of alloys. DMS materials, especially those with transition metal dopants over interesting ways to play physics with magnetic field interactions. These particular dopants tend to have the partially filled d-shell electron orbital states, which in theory, allow for new, typically forbidden, energy transitions which can improve overall performance. The doping of quantum dots with transition metals has been explored and shows that doped quantum dots can be particularly beneficial in photonic and optoelectronic devices (17). With this in mind, a specific area of interest regarding these quantum dots was the use of transition metal dopants such as a Mo-Mo dimer dopant. This specific dopant has not been rigorously studied and may prove useful based on prior results with other transition metals.

Now that the materials under investigation have been defined, it is pedagogically imperative to discuss band structures of common materials, p-n junctions, and optical transitions. To begin, we must answer a question: "What is band structure?" Without going into too much detail, band structure is a term associated with the description of allowed and forbidden energy levels where electrons can reside. Band theory describes the changes in the band structure as changes in the density of states (where electrons can exist) versus energy and/or momentum. The modeling of the electron orbitals maps out the valence band electron energy states and possible conduction band states. It also discusses forbidden energy levels, electrons can't go there, which

is commonly referred to as the bandgap region, but it could also refer to transitions governed by strict selection rules based on spin and momentum (18). The band structure of materials can be grouped into three categories namely: conductors, semiconductors, and insulators. These are defined by their conductivity and optical/electronic properties. A conductor is a material with charge carriers (positive or negative) that can flow with very little impendence in the presence of an applied electric potential or electric field. From the band structure point of view a conductor has overlapping conduction and valence bands, see figure 4. Typically, one thinks of conductors as being metals, and most are true metals, which has a bit different looking band structure (figure 4) as all electrons in a metal can conduct to produce a current. A semiconductor has charge carriers that will flow in the presence of an applied electric field but there are forbidden regions within its band structure, see figure 4. The bands are divided between the valence bands and the conduction bands. All of the states in the valence band or all states below the fermi level are filled with electrons that have the potential to excite to the empty conduction band states. The bandgap serves as an interesting tool because of the bandgap semiconductors are capable of absorbing light with energy greater in value than the energy of the bandgap to produce conduction electrons for use in an external load. In contrast to conductors and semiconductors, an insulator is a material with almost no free charges and cannot conduct charge to form a significant current. Insulators also have wide band gaps and usually won't absorb light below 5-6 eV in energy (18).

If one were to focus on the semiconductor category then these materials can be broken down further into two types, specifically intrinsic versus extrinsic semiconductors. The Fermi level define. (18) The Fermi level for an intrinsic semiconductor is located equally far from the conduction band and valence band edge near the middle of the band gap region. The type of extrinsic semiconductor is based on the relative position of the Fermi level with respect to the

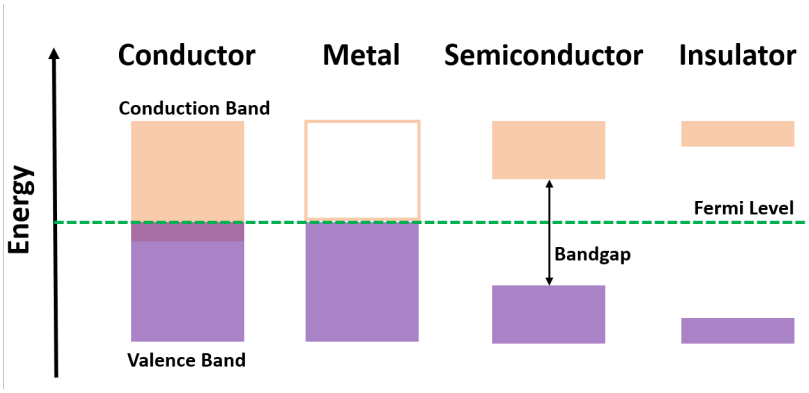

Figure 4: *Schematic of band structure for a conductor, metal, semiconductor, and insulator. Conduction band in pink and valence band is purple.*

conduction or valence band edges and is governed by the type of dopant, donors giving excess electrons or acceptors contributing excess holes. A p-type extrinsic semiconductor has holes (positive charge) as the majority carriers and the fermi level is closer to the valence band than the conduction band. An n-type extrinsic semiconductor has electrons (negative charge) as the majority carriers and the Fermi level closer to the conduction band edge. Figure 5 (a) gives a good idea at least a simple idea of the band structure and Fermi position for extrinsic and intrinsic type

semiconductors. When these types of semiconductors (dissimilar) are interfaced (touched) together the formation of a heterostructure occurs and is known as a p-n junction, see figure 5 (b). Upon interfacing, the p-type comes in contact with the n-type, charge carriers diffuse across the interface until an equilibrium condition is reached. The resulting charge transfer produces a depletion region with a built-in potential or electric field across the interface. The built-in potential is the difference in Fermi energy levels between the n-type and p-type materials before joining, or the difference in the conduction band levels after joining. The built-in potential field acts as a barrier to charge flow across the interface, but it can be used to separate photo-induced excitons which are formed inside or in close proximity to the depletion region and is discussed later. (18)

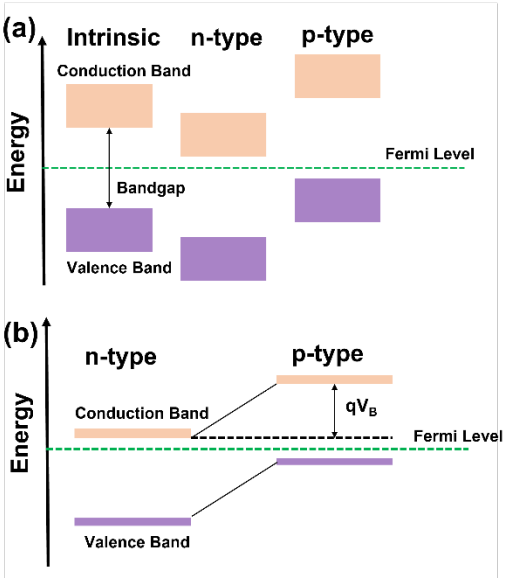

Figure 5: *Schematic of band structure for an (a) intrinsic vs extrinsic (n-type & p-type semiconductor and (b) for a p-n heterojunction. Conduction band is pink and valence band is purple.*

Now that a foundation for basic band structure has been established it will help for later discussion if the processes of absorption and luminescence are mentioned briefly. Absorption is defined as the process by which a photon is absorbed by a material. That energy excites an electron from the valence band to the conduction band forming an exciton (electron-hole pair). Luminescence is the reverse process of absorption and is defined as the decay or transition of an excited electron from the conduction band or trap state back into the valence band. This process is sometimes referred to as recombination and results in a photon being emitted but is not guaranteed as non-radiative (no photon) recombination is possible (18).

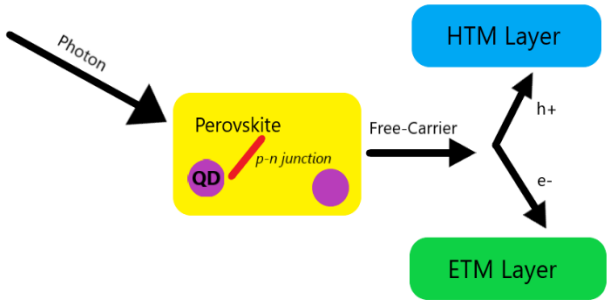

Figure 6: *Schematic of light absorption, exciton formation and charge extraction process within the p-n heterojunction solar cell.*

All of this sets the stage to understand precisely how the photovoltaic device operates. When the device is exposed to light, the perovskite layer and the quantum dots absorb photons and produce excitons. These excitons consist of an excited electron-hole pair. These are potential free carriers, which if close enough to a p-n junction or the built-in field at the interface of the quantum dots with the hybrid halide perovskite, are swept away to the electrodes to power some sort of electrical load. However, there is a chance the free carriers/ exciton recombines without producing current. The process of light absorption and charge collection is schematically illustrated for an HHP based solar cell in figure 6. Once light is absorbed, the exciton forms and is separated. The electrons are then transferred through the electron transport material (ETM) layer down to an ITO glass which is connected to a metal electrode.

On the other hand, the hole is conducted and transferred through the hole transport material (HTM) layer. The net creation and flow of charge results in the generation of a photocurrent in the outer circuit. These devices can be improved in several ways. A compact TiO_2 layer can be introduced to prevent short circuits between the top and bottom electrodes. The addition of a mesoporous TiO_2 layer can increase the light receiving area and improve the overall efficiency of the device (19). The addition of a quantum dot layer can improve the electron extraction efficiency and reduce the chance that free carriers recombine at the boundary between the ETM and the perovskite (20). When measuring the photo-response the solar cell behaves like a classical diode, but the light produces a non-zero current at zero bias and effectively shifts the diode curve along the vertical access. This can be described with the photodiode equation (21):

$$I = I_O\left(e^{\frac{qV}{nk_BT}} - 1\right) - I_L \quad (2)$$

Where I is the total current, I_o is the reverse saturation current, q is the electron charge, V is the applied bias voltage, k_B=1.38 x 10^{-23} J / K, is the Boltzmann Constant and T is the absolute temperature (273 K= 0 ºC), I_L is the photocurrent, and n is the identity factor. When I=0 then V=V_{OC} and when V=0 then I=I_L=I_{SC}. V_{OC} is the open circuit bias and is an indicator of the extent of recombination in a device. I_{SC} is the short-circuit current and gives the maximum photocurrent produced at zero bias. The goal of solar cell design and band engineering is to maximize the product of I_{sc} with V_{oc} to improve the overall performance. Now that the process of perovskite solar cell operation has been detailed, there remains one more key area to touch on.

The solar spectrum is a crucial part of device performance since the maximum light intensity resides in the visible spectrum, as shown in Figure 7. Accordingly, the ideal bandgap for a material absorbing in our solar spectrum would absorb all of the visible spectrum. This means a bandgap of less than 1.5 eV (> 827 nm) is ideally suited for our atmosphere. It is not a requirement but a good guiding principle. This caveat can be circumvented through interface engineering as possessing an ideal bandgap does not guarantee efficient charge extraction in device form.

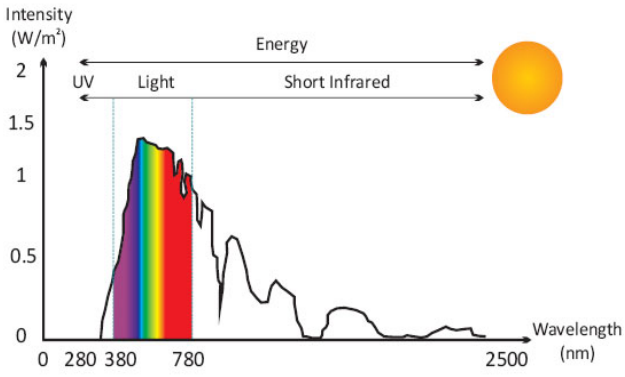

Figure 7: *Solar emission spectrum within earth's atmosphere, the diagram illustrates UV, Visible, and IR ranges of the emission spectrum, adapted from (22)*

Moreover, the intensity of the solar emission is different depending on if you are in space or within our Earth's atmosphere. The intensity is much higher outside the Earth's atmosphere; more about this is discussed at the end of chapter 3. This means that it is important to utilize materials that absorb this light the best in order to maximize device performance. The starting point is to have a material with optical bandgap energy less than that of the incident light to ensure photon absorption. The use of a proper material in the photon absorption layer of the device is imperative. If the material used does not absorb well in the visible spectrum, the device will not be as efficient as it could be and possibly not absorb light at all. In accordance with prior studies, it has been found that the hybrid halide perovskites have reliable absorption under the visible spectrum. The bandgap for thin-film $CH_3NH_3PbI_3$ has been reported in literature to be 1.55 eV, (23) thus well suited to absorb light in the visible range. In contrast, the optical bandgaps of ZnS have been reported to be 3.6-3.7 eV (335-344 nm) (24),

which implies without further bandgap engineering may not absorb well in the visible region and result in poor efficiency devices. The combination of all of these factors relating to device architecture, optical and electromagnetic properties, and chemical composition of various components allows for the creation of a viable solar cell that can be examined for potential benefits as they relate toward the future of clean energy and perovskite photovoltaics.

By way of introduction a sort of list regarding the efficacy and purpose of each material has been made and the key points will be listed below:

- Nanoparticle: This provides increased area for more charge extraction and higher charge extraction efficiency, i.e., it makes the p-n junction area larger.
- Band engineering: the nanoparticles have size-tunable bandgap properties controlled through growth temperature and introduction of a transition metal dopant
- p-n junction: a p-n junction is being employed to take advantage of a built-in electric field. Here, ZnS serves as the n-type material, and the HHP serves as the p-type material.
- Good absorbers: HHPs are good absorbers in the visible wavelength region and have reported high efficiencies, while ZnS quantum dots are good absorbers in the UV range.

Through the combination of these factors and careful bandgap engineering, it is proposed that the Mo_d:ZnS quantum dot devices will prove to outperform the ZnS quantum dot devices.

Chapter Two

Experimental Methods

Material Synthesis and Device Fabrication: Each device is based on the architecture in Figure 1. The creation of these perovskite solar cells involved the application of a five step, wet chemical process as described below. All substrates are indium tin oxide (ITO) coated glass sonicated in an Acetone ice bath for 15 min., followed by IPA ice bath for 15 min. and deionized (DI) water for 15 min. The substrates were then dried using gaseous ultra-high purity (UHP) nitrogen. The samples were then plasma etched for 2 min. in an oxygen plasma.

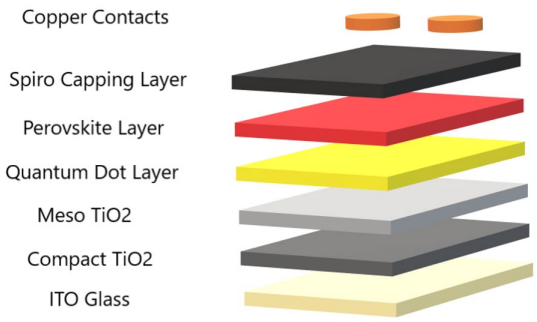

Figure 8: *Diagram representation of the solar cell architectures under investigation, there are 7 layers required to form a complete device.*

Compact TiO_2 Layer: In the first step, the substrates are moved to a glove box filled with UHP nitrogen. A compact TiO_2 layer of roughly 5-10 nm size nanoparticles was grown directly on the surface of the ITO-glass by first spin-coating a 20 uL droplet of a 0.15 M solution of Titanium diisopropoxide bis(acetylacetonate) (TdB) in 1-butanol at 4000 rpm for 30 seconds. The sample is then heated to 125 °C for 5 min. on a hot plate. Then using a 0.3M TdB 1-butanol solution two more spin-coating layers are deposited with subsequent heating to 500 °C for 15 min per layer. The samples were removed from the glove box and placed in a fume hood. Once in the fume hood the samples are immersed in a 40 mM $TiCl_4$-Toluene solution at 70 °C for 30 minutes on a hot plate in air. The samples are then rinsed in a 1:1 ratio DI water:ethanol solution. Finally, the samples are heated for 15 minutes at 500 °C allowing a reaction to occur which produces the compact layer on the ITO substrate and generate HCl gas as a byproduct. The resulting films of quality produce transparent textured films and upon heating, change to transparent pink-white color. The compact TiO_2 layer serves as both a hole blocking and electron transport material which helps to prevent short circuits from the top metal contacts and gives efficient charge extraction.

Mesoporous TiO_2 Layer: The second step involved the deposition of a Meso-TiO_2 layer on top of the first compact layer mentioned above. Mesoporous TiO_2 solution is created by combining 6 g of anatase TiO_2 30 nm particle powder with 10 mL of an ethanol/acetic acid solution. Then 0.2-0.9 mL of Triton X100 (surfactant), 0.2-5 mL of Ethylene glycol(surfactant/binder) are added to the TiO_2 mixture, and the solution is stirred for at least 5 hours or until all materials are well mixed. A layer of mesoporous TiO_2 is spin-coated onto the compact TiO_2 layer at 2300 rpm for 30 seconds. The cells were then annealed in air at 500 °C for 30 minutes. This forms a uniform white layer which is semitransparent. The mesoporous TiO_2 acts as a loading layer or a scaffolding for the quantum dots to infiltrate and attach too.

Quantum Dot Synthesis: Following the completion of this second step, two different varieties of quantum dots were used in the third step. The precipitation reaction was used to study the optical and structural properties of the ZnS and Mo-Mo dimer doped ZnS quantum dots. The quantum dots are the n-type semiconductor with size tunable electrical and optical properties. Their small size also increases the surface area of the heterostructure interface, i.e., QD-Perovskite.

A. Precipitation Reaction: The ZnS quantum dots were created through a precipitation reaction, depicted in Figure 9, whereby zinc acetate dihydrate (0.8662 g), was mixed with 40 mL of dimethyl sulfoxide (DMSO) in a three-neck round bottom flask. The solution is placed under vacuum and then UHP nitrogen via a Schlenk line and glass reflux tube attached to the three-neck flask. The solution is heated to 75 °C under constant stirring; once at temperature, a solution of Na_2S (0.1561 g), in 10 mL of deionized water was injected into the Zn acetate/DMSO solution and heated for 9 h under constant stirring and cool water refluxing. To precipitate out the QDs, a ratio of 1:6 mL of unprecipitated solution to acetone; was injected which causes the quantum dots to crash out of solution forming a white residue. The resulting powders were rinsed and centrifuged separately with methanol, and then isopropanol, three times each in order to sufficiently remove any unreacted precursors. Following the rinsing step, the powders were mixed with ethanol and used for optical and structural characterization. The Mo-Mo doped materials were made with the same process described above by adding appropriate amounts of Mo-Mo dimer acetate.

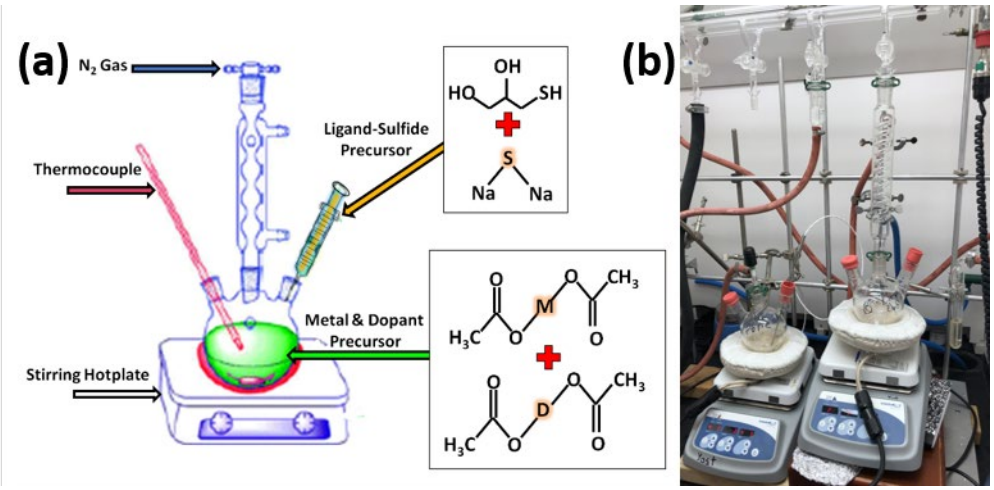

Figure 9: *(a) Schematic representation of the precipitation reaction for synthesizing quantum dots and (b) photo of experimental setup attached to a Schlenck line.*

B. SILAR Growth: The third step involved the cells undergoing direct growth deposition via successive ionic layer adsorption reaction (SILAR) method and a precision programmable dip coater, see figure 10. The Mo-Mo dimer doped and undoped ZnS quantum dots were grown for one, three, and five cycles. A single SILAR cycle consists of dipping the above sample into a cationic solution of Zn acetate dihydrate (0.275 g) in 1:1 Ethanol:DI Water (50 mL), followed by dipping into a rinse solution of 1:1 Ethanol:DI Water (50 mL) to remove any unreacted materials, then dipping in an anionic solution of

Na_2S (0.1561 g) in 1:1 Ethanol:DI Water (50 mL), followed by dipping into a rinse solution of 1:1 Ethanol:DI Water (50 mL). For the Mo-Mo dimer doped quantum dots, 0.0165 g of Mo-Mo dimer acetate was added to the Zn acetate dihydrate solution. Following the completion of the SILAR method cycles, both cells were transferred to a glovebox for the remaining steps.

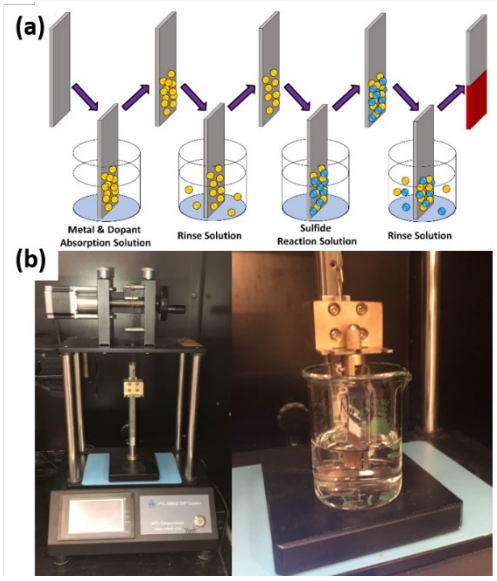

Figure 10: *(a) Schematic representation of a single SILAR cycle for coating quantum dots onto the TiO_2 layers and (b) photo of experimental setup with dipcoater and zoomed image of film being coated in quantum dot thin film.*

$CH_3NH_3PbI_3$ Synthesis: A hybrid halide perovskite was synthesized in a glove box under UHP nitrogen, figure 11, using 461 mg of PbI_2, 159 mg of MAI, and 1.25 mL of DMF, which was stirred for two hours at 60 °C. The perovskite was then deposited on the cells via spin coating at 3000 rpm for 30 seconds. The cell was then annealed at 90 °C for two hours. A second layer is coated at 1500 rpm for 30 seconds and heated to 90 °C for one hour. The hybrid halide perovskites serve as the p-type semiconductors. This means that operation occurs in a p-n junction solar cell/device physics. The p-n junction gives a built-in potential for charge/exciton separation.

Spiro-C Synthesis: The fifth synthesis step involved creating a hole transport layer known as Spiro-C. Spiro-C is made by combining 180 mg of Spiro-MeOTAD with 1 mL of chloroform and stirring until all material is well dissolved. Then 7 uL of 1:26 ratio uL/mg of Tertbutylpyridine is added to the above solution under constant stirring. Next, 15 uL of a 170mg/mL of Lithium bis(trifluormethanesulfonyl)imide (LiTFSI)/Acetonitrile solution is added to the above solution then heated at 70 °C for 30 minutes with constant stirring. A thin layer is formed via spin-coating at 4000 rpm for 30 seconds in a glovebox under UHP. The samples are allowed to cure for 12 hours before metal electrode deposition. This layer was applied to prevent environmental degradation from occurring in the perovskite layer. In addition to this, the Spiro-C layer acts as an electron blocking and hole conducting layer as well as helps to prevent degradation and allow for efficient charge extraction. Following the successful application of the layer, the cells were then removed from the glovebox.

Figure 11: *Photo of double glove box with spin-coater and heater for air sensitive synthesis of the hybrid halide perovskite and hole transport layers.*

Metal Electrode Deposition: A process of metal evaporation was then used to create copper contacts on the surface of each cell to test cell efficiency. A mask was created to ensure each cell had two equally sized contacts deposited. The metal evaporation took place under vacuum at pressures around 10^{-6} Torr and lasted for ninety seconds for each cell. These contacts serve as the point of measurement for each cell.

Figure 12: *Photo of the TEM used to characterize the size of nanoparticles*

Device Characterization: Following this, photo transport measurements were performed to assess the role of dopant and the number of SILAR cycles with respect to performance. Current measurements were taken for each cell using a 2401 Keithley Source Meter at room temperature. The light source, an Oriel Corporation Xe Arc Lamp, was focused on each cell, and the intensity of the light from bulb ranged from 100 W/cm^2, 120 W/cm^2, and 150 W/cm^2.

X-ray Diffraction (XRD): The crystal structure for the quantum dots and the perovskite thin films was measured using a Rigaku Smartlab Diffractometer. The wavelength used was from Cu Kα with λ=1.54 Å. All XRD was performed in air at room temperature.

Transmission Electron Microscopy (TEM): quantum dot samples were prepared via precipitation method and then suspended in ethanol. A droplet of the suspension was placed onto a carbon-coated TEM grid. TEM data was acquired through the use of a JOEL JEM-2100 Scanning Transmission Electron Microscope operating at 200kV accelerating voltage, figure 12.

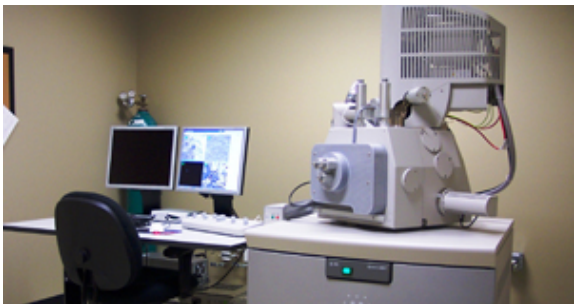

Figure 13: *Photo of SEM used to characterize the morphology of the perovskite thin films grains and grain boundaries*

Scanning Electron Microscopy (SEM): the morphology of the $CH_3NH_3PbI_3$ thin films was explored with special emphasis on grain size and grain boundary density. This was accomplished through the use of a FEI Quanta 600 field emission gun environmental scanning electron microscope at an accelerating voltage of 20 kV unless otherwise indicated, figure 13.

Optical Absorption Spectroscopy: Quantum dots grown by the precipitation reaction were extracted as powders and dried at room temperature. Once in dry powder form the powders were redispersed in a solution of ethanol or isopropanol and placed in a cuvette for optical characterization. Optical absorption spectroscopy was performed in the UV-Visible range and acquired using a DU 530 Beckman Colter UV-Visible spectrophotometer.

Chapter Three

Results and Discussion

Crystallinity: As the size of a material transitions from bulk to the nanoscale the extent of lattice periodicity reduces. The reduction in periodicity can cause phase changes or reorientations in the overall crystal structure. Subsequently, the symmetry changes and possibly the material's optical and electronic band structures. Thus, it is instructive to quantify the crystal structure and symmetry of the nanoparticles and films to be used in the solar cells. XRD measurements were taken for several components that made up the devices. As shown in figure 14 (a), the non-normalized diffraction pattern for ZnS (green curve) quantum dots exhibits three broad peaks located at roughly 29°, 48°, and 57° which closely matches previous results (25) and suggests the ZnS quantum dots form in a zinc-blende structure. The XRD profile for Mo_d:ZnS is also shown in figure 14 (a) but the three main peaks are shifted to slightly higher 2θ as compared to the ZnS profile. Additionally, in the Mo_d:ZnS a smaller shoulder peak appears located at roughly 34°. These data, although similar, suggest that incorporation of the Mo_d dopant does decrease the lattice constant and introduce some new lattice planes not observed in the undoped ZnS system.

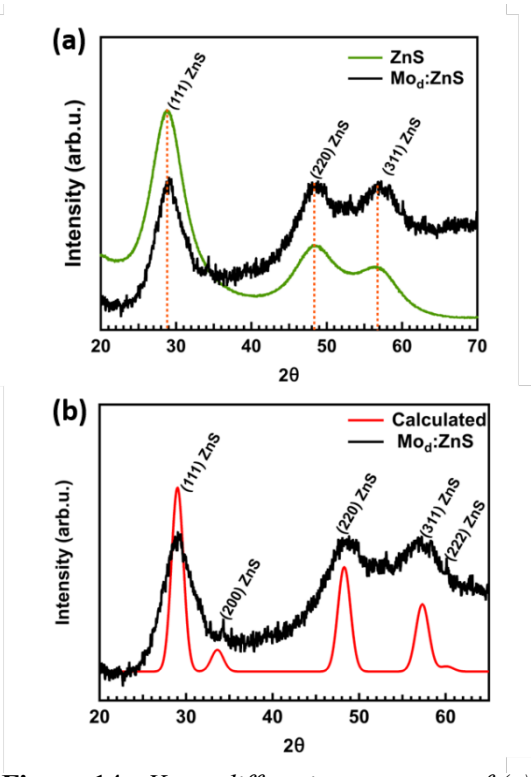

Figure 14: *X-ray diffraction spectrum of (a) undoped ZnS and Mo_d:ZnS and (b) Mo_d:ZnS and calculated XRD for ZnS quantum dot of 5 nm diameter.*

To explore the difference between the XRD profiles a model of undoped zinc-blend (f-43m point group symmetry) ZnS with width of 5.0 nm was created and the calculated XRD pattern for zinc-blend ZnS quantum dots (red curve) is shown in figure 14 (b) in comparison to the Mo_d:ZnS (black curve). The calculated XRD has five peaks located at 29°, 33.62°, 48.28°, 57.31°, and 60.11° which correspond to the (111), (200), (202), (131) and (222) crystal planes of ZnS, respectively. The unit cell from the model is a = b = c = 5.3275 Å and α = β = γ = 90° and together with the diffraction pattern can be used to create a ball and stick model of the calculated ZnS crystal, see figure 15. The XRD profile of the Mo_d doped ZnS quantum dots match closely to the calculated XRD profile for 5 nm ZnS quantum dots. Further calculations with Mo_d dopant are needed as discussed in chapter 4.

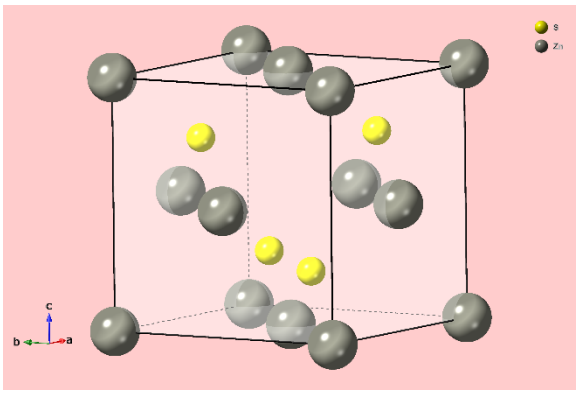

Figure 15: *Ball and stick model diagram compiled from calculated XRD pattern for ZnS quantum dot of 5 nm diameter.*

The similarity between the Mo_d:ZnS xrd profile and the calculated XRD profile implies the

introduction of the dopant doesn't change the symmetry but does change the crystallinity slightly. The change in crystallinity is defined with the appearance of the shoulder peaks due to the (200) and (222) ZnS lattice planes effectively making the Mo_d:ZnS possibly more polycrystalline or larger in size as compared to the undoped ZnS (Figure 14 (a)). From this perspective it could be safe to assume, that any changes in optical or electronic properties will not be related to crystal structure or symmetry but to size or crystallinity.

Briefly, the broadening in all the peaks is expected and reflects the small size of the nanoparticles and edge effects due to small periodicity in the diffraction path. The Debye-Scherrer equation (26):

$$\tau = \frac{k\lambda}{\beta \cos\theta} \tag{2}$$

where τ is the average size of domains, grains or particles, k is the shape factor related to the physical shape of the nanoparticles, λ is the X-ray wavelength, β is the full-width at half-maximum (FWHM) of the diffraction peak, θ is Bragg angle (26); describes broadening effects in XRD profiles associated with small crystallite size and sometimes can be used to determine particle size in powders. Unfortunately, using the FWHM of any of the peaks in figure 14 (a) to compare particle sizes between doped and undoped ZnS proves difficult. The difficulty in comparison is mostly due to the differences in peak position and overlapping peaks in the Mo_d:ZnS profile.

The $CH_3NH_3PbI_3$ thin films and meso-TiO_2 films were measured separately from the quantum dots as these films are polycrystalline and exhibit many diffraction peaks that tend to dominate the quantum dot profiles. The diffraction patterns are shown in figure 16. Extreme care must be taken when synthesizing $CH_3NH_3PbI_3$ in order to get a proper perovskite structure, a slight deviation in the precursor masses/ratios can result in very different phases dubbed pseudo perovskites (27), namely due to the presence of off stoichiometry contributions and precursor peaks as a result of degradation or poor mixing. The results in figure 16 suggests $CH_3NH_3PbI_3$ adopts a preferred (110) direction with tetragonal phase symmetry and I4/mcm space group (28) In comparison the meso-TiO_2 adopts an anatase crystal structure which is the preferred structure due to ideal bandgap offset, electron mobility, and stability in solar cells (29) which is necessary 1) for blocking holes and allowing electrons through to the ITO electrode and 2) to prevent short-circuiting between the top metal contact and the transparent ITO electrode. In accordance with the XRD profiles of the different crystalline layers our device materials and associated recipes produce high quality films (30). The crystal structure of the perovskite films grown in this project match films of high performing devices from literature (30). Furthermore, the sharp peaks indicate

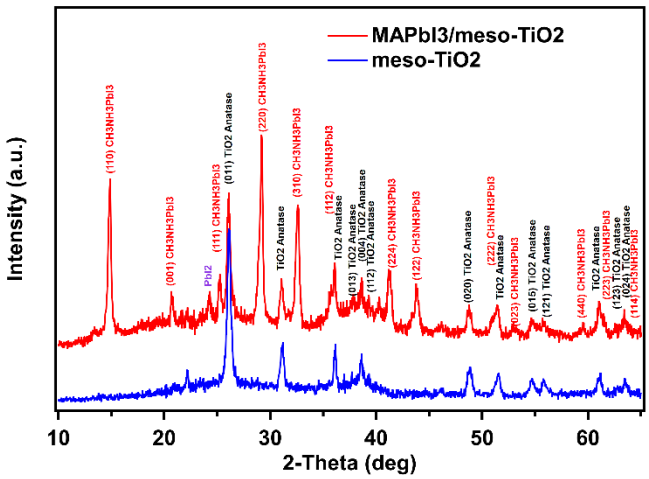

Figure 16: *X-ray diffraction spectra for $CH_3NH_3PbI_3$ and meso-TiO_2 thin film layers.*

possible large grain polycrystalline films which can be checked using scanning electron microscopy.

Nanoparticle Size and Perovskite Film Morphology: The size of both the doped and undoped quantum dots was important to examine as it could be a factor in device performance discrepancies stemming directly from differences in optical and electronic bandgaps. TEM data was taken for both sets of quantum dots, as shown in figure 17.The lattice fringes can be observed in some of the quantum dot surfaces, highlighting the high resolution of the TEM instrument and high quality of the nanoparticles. Several dozen quantum dots were analyzed to determine their respective size distribution. A histogram of the size distribution data is shown in figure 17 (c) and indicates the ZnS quantum dots are approximately 3.1-4.1 nm in diameter while the Mo_d:ZnS quantum dots are roughly 4.2-5.8 nm in diameter. The Mo_d doped quantum dots are larger on average by about 1 nm, and the size distribution is larger as compared to the undoped ZnS and other transition metal-doped quantum dots. It is important to mention, although not shown, that the other transition metal doped ZnS quantum dots, Mn, Co, and Ni, had similar sizes to the undoped ZnS. The size difference is most likely related to differences in temperature during growth and requires a closer look and possible reevaluation of the temperature control methods used, as discussed in chapter 4.

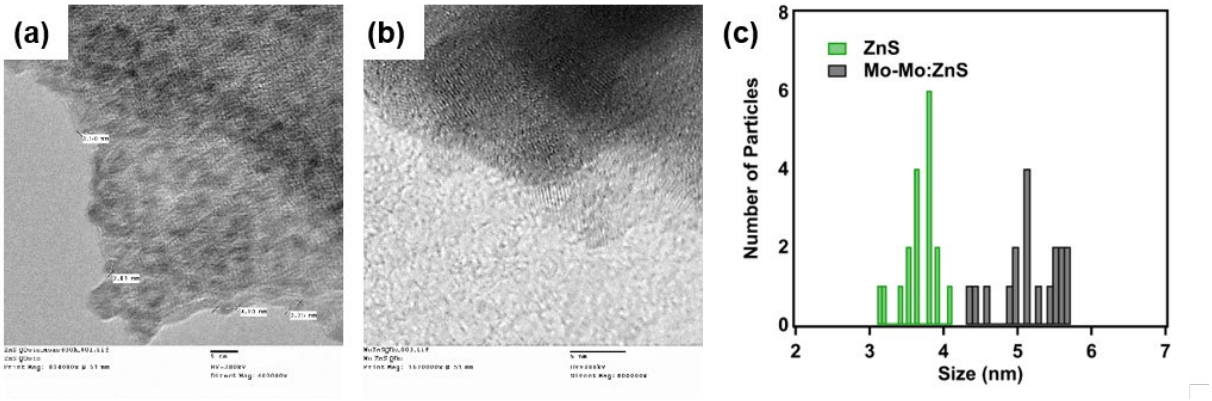

Figure 17: *Transmission electron microscopy image of (a) undoped ZnS with measurements, (b) Mo_d:ZnS quantum dots attached to carbon coated copper TEM grid and (c) a histogram of size distribution for Mo_d:ZnS and undoped ZnS quantum dots grown using precipitation reaction method.*

It is thought that grain size and hence grain boundary density contributes to overall performance of the photovoltaic properties in the hybrid halide perovskites (HPP) (8). Due to the important nature of the grain size it proved useful to measure the morphology of the surfaces using scanning electron microscopy. Figure 18, shows and SEM image of the surface of a typical $CH_3NH_3PbI_3$ film observed from our synthesis recipe. Notice the grain sizes are on the order of 20-50 nm and some grains are rather large (100 nm in width) but not at high density as compared to the smaller grains. The linear grain boundary density can be approximated knowing the size of the image and the average range in grain size. A rough approximation puts the linear grain boundary density at 22-54 grain boundaries per 1.0 μm. This is a high grain boundary density as the size of grains for high performing HHPs is typically closer to above 100-150 nm in width. The morphology, grain size and density were similar amongst all the devices and films. Although some areas looked strange with features resembling bowtie like texture shown in figure 18 (b). The

bowtie features were observed around the surface of every HHP film but the majority of the surface was small grain morphology. Further measurements and modeling are needed to understand these neat features.

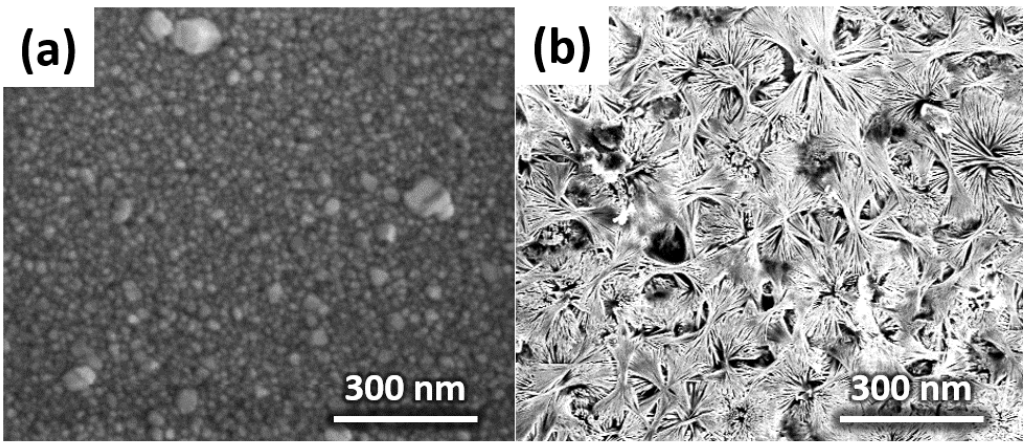

Figure 18: *Scanning electron microscopy image of the surface of a typical $CH_3NH_3PbI_3$ thin film grown on top of ZnS quantum dots/meso-TiO_2/c-TiO_2/ITO-glass. (a) small grain size texture is seen around most of the surface, avg. grain size =35 nm and (b) strange bowtie-like structures formed at the surface in different patches, bowties are 200-300nm across.*

Optical Response: as mentioned earlier in the introduction, the size-dependent properties of quantum dots offer an opportunity for band gap engineering. Bandgap engineering is simply the manipulation of a material's optical/electronic bandgap via changes in size, composition (doping), crystal structure etc. in order to produce a favorable bandgap value. It is a useful tool for tuning a photovoltaic material to absorb across larger portions of the solar spectrum. Bandgap engineering is similar to interface engineering. Interface engineering is the manipulation of bandgaps and the associated offsets between conduction and valence bands at an interface of two materials. It has been shown that transition metal dopants can heavily influence the band structure. Recently it was shown that doping Mn into ZnS and CdS can produce in-gap states associated with the Mn dopant. In Mn:PbS quantum dots, a 700% increase in photocurrent was measured while a decrease in absorption was seen with nominal doping of Mn (31). This large increase was attributed to the large wavefunction overlap of the Mn dopant with the charge conduction channel. To test the original hypothesis that Mo_d:ZnS should perform better we must first check that they absorb light better, and this can be evaluated through optical absorption spectroscopy.

Optical absorption (OA) spectroscopy measures how well a material absorbs over a broad wavelength range. The response for dilute solutions will give information about the formation of the excitons, the onset of absorption and the optical band gap (32). Furthermore, OA spectroscopy can be used to detect in-gap states created by dopants or other defects. As shown in Figure 19, the OA spectra for several transition metal-doped ZnS quantum dots indicate that Mn, Co, Ni, and Mo_d dopants increase absorption over the measured visible wavelength range compared to undoped ZnS. This has been observed and predicted in literature (33). Additionally, there are many exciton shoulder peaks and in-gap states created by introducing transition metal dopants. From the

OA data it is difficult to make conclusions about the bandgap but by plotting the OA data in a Tauc plot we can extrapolate the bandgap energies. Before discussing the data further, it is good to discuss how to make the Tauc plot.

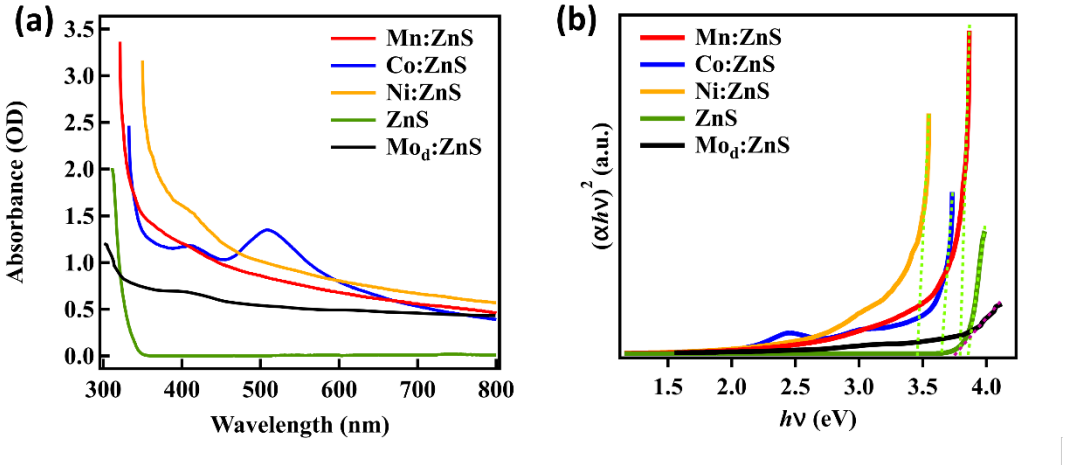

Figure 19: *(a) Optical absorption spectra for undoped and transition metal doped ZnS quantum dots and (b) the corresponding Tauc plots of the optical absorption spectra.*

In order to determine the onset of absorption or bandgap, it is useful to make a Tauc plot and then extrapolate the bandgap from the linear portion of the Tauc plot. This method is based on the following formula (34)

$$(\alpha h\upsilon)^{1/\gamma} = A(h\nu - E_g) \tag{3}$$

where α is the energy-dependent absorption coefficient, h is the Planck constant, ν is the photon's frequency, E_g is the average band gap energy of the material, and A is the band tailing parameter. The index factor, γ, depends on the nature of the electron transition and is equal to 1/2 or 2 for the direct and indirect transition band gaps, respectively. This allows one to extract the direct bandgap from the Tauc plot and explore the effects of transition metal dopants on ZnS optical band structure. It appears the introduction of transition metal dopants reduces the bandgap of ZnS but recall the Mo$_d$:ZnS was roughly 1 nm larger than the other quantum dots. It is not fair to say that the introduction of Mo$_d$ dopants was the sole cause for the reduction of the bandgap as quantum confinement and size also played a role. The results for the bandgaps extracted from the Tauc plot are listed in table 1.

Material	**Optical Bandgap (eV)**
ZnS	**3.85**
Mn:ZnS	**3.79**
Co:ZnS	**3.65**
Ni:ZnS	**3.46**
Mo$_d$:ZnS	**3.74**

Table 1: *Optical energy gaps extracted from the Tauc plot in figure 18 (b).*

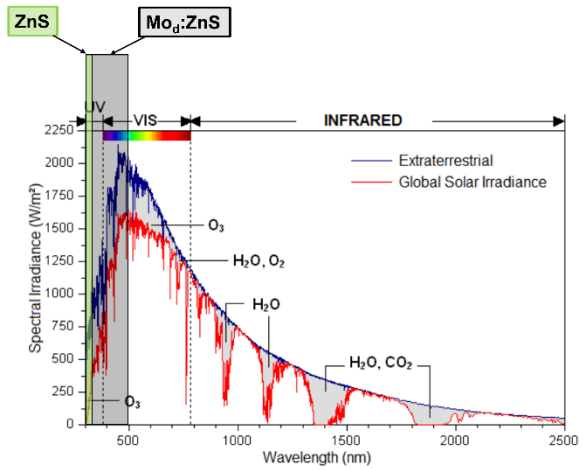

Figure 20: *Solar spectrum comparison for emission inside earth's atmosphere (red curve) vs outside the earth's atmosphere (blue) curve. Over plotted transparent boxes are range of allowed/enhanced absorption for ZnS and Mo$_d$:ZnS quantum dots as measured by optical absorption spectroscopy in figure 19. Figure adapted from (35)*

Closer inspection of the extracted bandgaps indicates that ZnS can only absorb light with energy above 3.85 eV (322 nm), which is in the ultra-violet region of the electromagnetic spectrum. Similarly, Mo$_d$:ZnS has a bandgap of 3.74 eV suggesting it can absorb effectively above 331 nm which is also in the UV region. The reader should notice the higher absorbance of the Mo$_d$:ZnS between the regions of 3.7 and 2.5 eV (335-496 nm) of the Tauc plot, as compared to ZnS. More than half of the region of enhanced absorption lies in the high intensity portion of the solar spectrum see figure 20. Additionally, looking at the OA spectra, it is clear that the transition metal doped quantum dots absorb light better across the whole range. So, where ZnS is not absorbing well or can't due to bandgap limitations the Mo$_d$ZnS is absorbing due to size and dopant induced differences in the band structure. Most of these modifications in the band structure have been attributed to strong sp-d exchange interactions, see ref (25). Based on these observations it is safe to predict that the reduced bandgap and enhanced absorption of the Mo$_d$:ZnS will result in better performance when in device form. To test this a device needs to be made and the photovoltaic response measured.

Photovoltaic Response: One of the most important benchmarks of a photovoltaic material or heterostructure is the process of photo induced carrier generation and recombination. Photo induced transport measurements are well understood and allow a researcher to assess quality of a material especially with respect to the changes in performance related to dopants and defects. A simple method to assess a photocell's efficacy is to perform current-voltage measurements under illumination from a Xe arc lamp. The radiative emission spectrum of the Xe arc lamp closely mimics the radiative emission spectrum of the sun and is thus a useful photo excitation source. In this project, the photocurrent produced by the Xe arc lamp is measured while the bias is ramped from -1.0 to 1.0V under illumination.

Once the devices were fabricated a series of several dozen samples were measured over several different contacts and the I-V profiles were averaged and corrected for bias direction. In figure 21, the resulting I-V curves for five devices at four separate light intensities are shown. These data suggest a few things about the solar cells and materials used. Let's begin by discussing the changes in I_{sc}. For the ZnS system the maximum value of the I_{sc} decreases with increasing number of SILAR cycles, whereas the I_{sc} of Mo$_d$:ZnS increases with increasing number of SILAR cycles. Additionally, the maximum photocurrent is higher for the undoped ZnS samples until five SILAR cycles are complete, at which point the layers of the device broke down and degraded before measurements could be taken. This rapid breakdown at high SILAR cycle number could be due to the formation of ZnO at the surface and subsequent annealing step. ZnO is known to be incompatible with HHP and results in deprotonation (removal of the hydrogen containing species)

and rapid material breakdown post annealing (36). The five cycle Mo_d:ZnS remained stable and outperforms all other samples. Next let's examine the changes in the V_{oc}. In both the ZnS and the Mo_d:ZnS systems the maximum V_{oc} increases with increasing number of SILAR cycles and on average the V_{oc} for Mo_d:ZnS is consistently higher than undoped ZnS at all light intensities.

A question arises about what could be causing the increase or decrease in the I_{sc} and V_{oc}. The fluctuations of the I_{sc} and V_{oc} are in part related to density of trap states at interfaces which lead to non-radiative recombination of the excitons. These trap states are usually caused by high grain boundary densities of the perovskite materials. The trap states can dramatically reduce the maximum I_{sc}. The fluctuations are also related to dopant states, introduced by the Mo_d, which

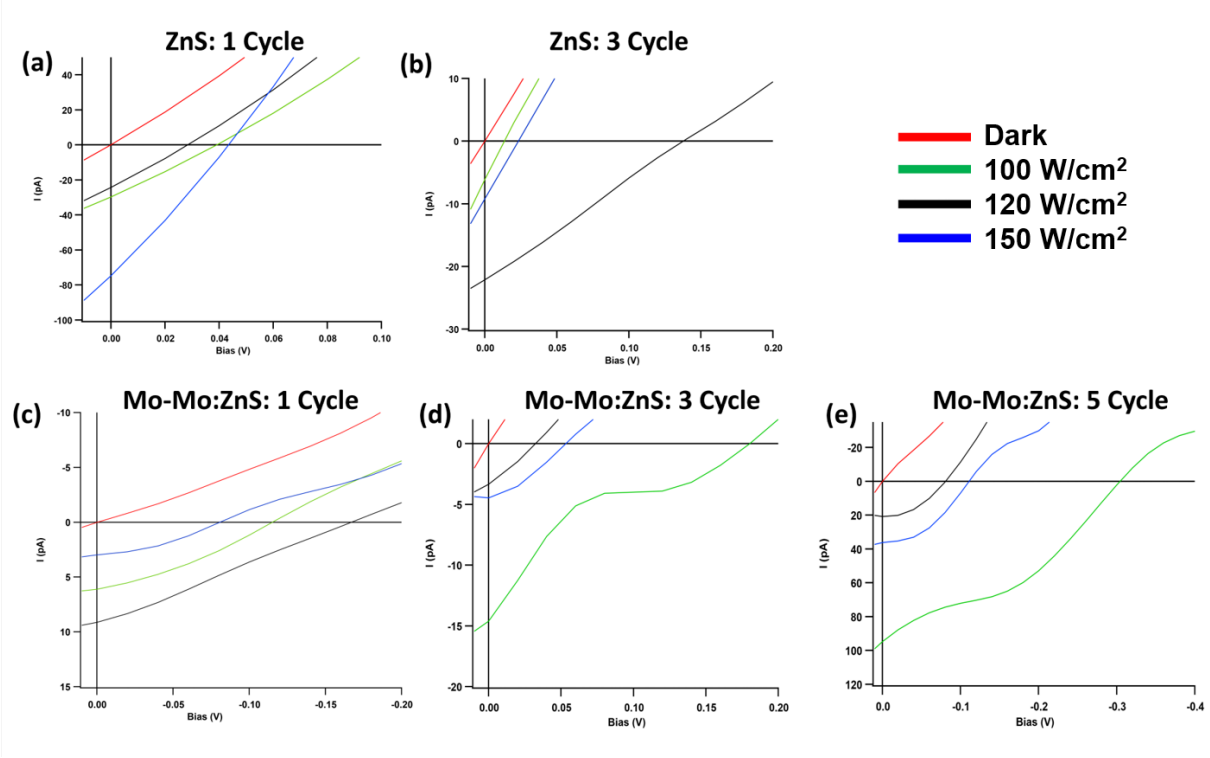

Figure 21: *I-V measurements for undoped ZnS/hybrid halide perovskite solar cells (a) 1 SILAR cycle of ZnS, (b) 3 SILAR cycles of ZnS, and for Mo_d:ZnS/hybrid halide perovskite solar cells (c) 1 SILAR cycle of Mo_d:ZnS, (d) 3 SILAR cycles of Mo_d:ZnS, and (e) 5 SILAR cycles of Mo_d:ZnS. The legend shows the four light intensities used Dark (red line), 100 W/cm^2 (green line), 120 W/cm^2 (black line), and 150 W/cm^2 (blue line).*

may lead to favorable charge extraction pathways across the p-n junction. Furthermore, if the interfaces/layers in the device have defects or gaps then short circuiting between the top metal electrode and bottom transparent electrode is likely and will reduce the V_{oc}. It has been shown that grain boundaries in perovskite based solar cells are not really responsible for reducing the V_{oc} (37), but the thickness of the perovskite can reduce overall photocurrent when less than 100 nm (38,39). In the present case the as the V_{oc} and I_{sc} improve with increasing Mo_d:ZnS SILAR cycles, then the non-radiative recombination due to trap states seems to be passivated with introduction of the Mo-Mo dimer. Recently, it was shown that similar growth conditions lead to ZnS and CdS quantum dots with many surface Zn- and S- vacancies (25). The presence of vacancy defects could lead to non-favorable trap states in the undoped ZnS. Upon incorporation

of the Mo-Mo dimer the trap states/vacancy defects are filled and potentially results in more favorable absorption and charge extraction.

It is worth noting the slope changes or bumps in the I-V curves. These bumps are common in perovskite I-V measurements and have been associated with ion migration or phase changes near the interface (40-42). This can be controlled with more sophisticated electronic source meters.

An interesting feature observed in the I-V data was how the overall curves changed with changing light intensity. Typically, when light of increasing intensity impinges on a photovoltaic cell the overall power output should increase linearly, increasing I_{sc} and V_{oc}. Thus, all of the devices should perform the best at 150 W/cm^2, but this is not the case. For example, the undoped ZnS system didn't appear to have preference for a particular light intensity, as the one SILAR cycle devices performed better at 150 W/cm^2 and the three SILAR Cycle performed better at 120 W/cm^2. In contrast, there was an apparent trend for the Mo_d:ZnS system which seemed to perform best under the 120 W/cm^2 light intensity for three SILAR cycles and higher. As mentioned previously, the Mod:ZnS has a smaller band gap and covers a region in the visible spectrum with higher intensity light than in the UV region. This means Mo_d:ZnS system is capable of accessing, through bandgap and interface engineering, more of the high intensity portion of the solar spectrum but may not be ideally suited as solar cell components on satellites outside of Earth's atmosphere, see figure 20.

In conclusion, size difference, dopant difference, defect/trap density difference are all potentially contributing to the trends we see, we believe the improved performance of the Mo_d:ZnS at five SILAR cycles is related to the reduction energy gap and of trap states, and increased number of p-n junctions between the quantum dots and HHP.

Chapter Four

Recommendations and future directions

These results both provide valuable insights into ways to improve solar cell efficiency and also raises new questions that can be explored moving forward. The IV results clearly show that the increase in SILAR cycles results in a more efficient device up to five cycles. It may be worth exploring if there is a point of diminished return with the SILAR process, perhaps at around seven to ten cycles. Since the Mo-Mo dimer doped system performed better, it may be worth comparing to another dimer doped or single doped systems to examine how the structure and makeup of the quantum dots can affect device performance. Changing the concentration of the Mo_d dopant from 1, 2, 5 10, 15, 20% could give more insight into the source of I_{sc} and V_{oc} improvement as it relates directly to the dopant. In addition to this, one unforeseen phenomenon to investigate moving forward was in relation to the copper contacts on the surface of the devices. Immediately following the completion of the metal evaporation, the copper contacts were a solid bronze color but after a day, even in a small gel-pak case, the contacts had begun to turn green as if they were rapidly oxidizing. This may affect device performance and exploration of this in the future would be beneficial. The five SILAR cycle ZnS system led to rapid decay of the perovskite films and this should be refabricated and remeasured to see if it was an error in environmental conditions during growth.

More modeling and theory calculations with Mo_d dopant incorporated are necessary for the XRD analysis. DFT calculations would be useful to understand more about the optical absorption and band structure. Temperature dependent IR and Raman measurements would be useful to explore the effects of phonons and other "vibrational" states and how those can serve to further manipulate the band alignment in the interface of the different heterostructures.

Improvements in experimental design should be focused on temperature control during growth. It is suggested that a P-I-D based temperature controller with better thermal housing should be used in the future to get better size control and size distribution. Also, additional steps of outgassing and filtration of the solvents and precursor solutions may help narrow the size distribution and improve crystallinity. Finally, the introduction of different ligands would open up more parameter space for tuning the band structure.

References:

(1) IPCC, 2018: Global Warming of 1.5°C. *An IPCC Special Report on the impacts of global warming of 1.5°C above pre-industrial levels and related global greenhouse gas emission pathways, in the context of strengthening the global response to the threat of climate change, sustainable development, and efforts to eradicate poverty,* Masson-Delmotte, V., P. Zhai, H.-O. Pörtner, D. Roberts, J. Skea, P.R. Shukla, A. Pirani, W. Moufouma-Okia, C. Péan, R. Pidcock, S. Connors, J.B.R. Matthews, Y. Chen, X. Zhou, M.I. Gomis, E. Lonnoy, T. Maycock, M. Tignor, and T. Waterfield (eds.), In Press. (2018).

(2) Kaufman, D., McKay, N., Routson, C. *et al. Holocene global mean surface temperature, a multi-method reconstruction approach. Sci. Data* **7,** 201 (2020). https://doi.org/10.1038/s41597-020-0530-7

(3) Kahan, Ari. *U.S. Energy Information Administration - EIA - Independent Statistics and Analysis Projected Growth in CO_2 Emissions Driven by Countries Outside the OECD* - Today in Energy - U.S. Energy Information Administration (EIA), U.S. Energy Information Administration, (16 May 2016), https://www.eia.gov/todayinenergy/detail.php?id=26252.

(4) Crabtree, George and Lewis, Nathan, *Solar Energy Conversion*, Physics Today. 60, (2007). DOI:10.1063/1.2718755.

(5) Nadel, Steven. *American Council for an Energy-Efficient Economy*, (2017), Natural Gas Energy Efficiency: Progress and Opportunities, https://www.aceee.org/sites/default/files/publications/researchreports/u1708.pdf.

(6) D. Shi, V. Adinolfi, R. Comin, et al, *Low trap-state density and long carrier diffusion in organolead trihalide perovskite single-crystals*, Science **347,** 519-522, (2015). DOI: 10.1126/science.aaa2725

(7) Wells, H.L. (1893*), Über die Cäsium- und Kalium-Bleihalogenide*. Z. Anorg. Chem., 3: 195-210. https://doi.org/10.1002/zaac.18930030124

(8) Vidyasagar, C.C., Muñoz Flores, B.M. and Jiménez Pérez, V.M. *Recent Advances in Synthesis and Properties of Hybrid Halide Perovskites for Photovoltaics.* Nano-Micro Lett. **10,** 68 (2018). https://doi.org/10.1007/s40820-018-0221-5

(9) Sato, T., Takagi, S., Deledda, S. *et al. Extending the applicability of the Goldschmidt tolerance factor to arbitrary ionic compounds*. Sci. Rep. **6,** 23592 (2016). https://doi.org/10.1038/srep23592

(10) *Perovskite Solar Cell*, Clean Energy Institute, University of Washington, (1 June 2020), https://www.cei.washington.edu/education/science-of-solar/perovskite-solar-cell/

(11) Jeong, J., Kim, M., Seo, J. et al. *Pseudo-halide anion engineering for α–$FAPbI_3$ perovskite solar cells*, Nature **592**, 381–385 (2021). https://doi.org/10.1038/s41586-021-03406-5

(12) Xiao, K. , Lin, R., Han, Q. et al. *All-perovskite tandem solar cells with 24.2% certified efficiency and area over 1cm^2 using surface anchoring zwitterionic antioxidant*, Nat. Energy 5, 870-880 (2020). https://doi.org/10.1038/s41560-020-00705-5

(13) Al-Ashouri, A., Kohnen, E., Li, B. et al., *Monolithic perovskite/silicon tandem solar cell with >29% efficiency by enhanced hole extraction*, Science 370, 1300–1309 (2020). DOI: 10.1126/science.abd4016

(14) Jošt, M., Kegelmann, L., Korte, L., Albrecht, S., *Monolithic Perovskite Tandem Solar Cells: A Review of the Present Status and Advanced Characterization Methods Toward 30% Efficiency*. Adv. Energy Mater. 10, 1904102, (2020). https://doi.org/10.1002/aenm.201904102

(15) Cotta, M. A. *Quantum Dots and Their Applications: What Lies Ahead?,* ACS Applied Nano Materials 3 (6), 4920-4924, (2020). DOI: 10.1021/acsanm.0c01386

(16) Ramalingam, G., Kathirgamanathan, P., Ravi, G., et al., *Quantum Confinement Effect of 2D Nanomaterials, Quantum Dots - Fundamental and Applications*, Faten Divsar, IntechOpen, (2020). DOI: 10.5772/intechopen.90140.

(17) Sharma, D., Malik, B.P., and Gaur, A., *Two and four photon absorption and nonlinear refraction in undoped, chromium doped and copper doped ZnS quantum dots*, J. Phys. Chem. Sol., 87, 163-170, (2015).https://doi.org/10.1016/j.jpcs.2015.08.011.

(18) Kittel, Charles. *Introduction to Solid State Physics*. 8th ed., Wiley, 2004.

(19) Zhou, D., Zhou, T., Tian, Y. et al., *Perovskite-Based Solar Cells: Materials, Methods, and Future Perspectives*, J. Nanomaterials, 2018, 8148072, (2018). https://doi.org/10.1155/2018/8148072

(20) Xie, J., Huang, K., Yu, X. et al., *Enhanced Electronic Properties of SnO_2 via Electron Transfer from Graphene Quantum Dots for Efficient Perovskite Solar Cells*, ACS Nano, 11 (9), 9176-9182, (2017). DOI: 10.1021/acsnano.7b04070

(21) Luque, A. and Hegedus, S. (Eds.), *Handbook of Photovoltaic Science and Engineering*, John Wiley and Sons Ltd., England (2003).

(22) Ushasree, P. M. and Bora, B. CHAPTER 1: Silicon Solar Cells, in *Solar Energy Capture Materials*, 2019, pp. 1-55 DOI: 10.1039/9781788013512-00001

(23) Lee, M.M., Teuscher, J., Miyasaka, T. et al., High Efficiency Hybrid Solar Cells Based on Meso-Superstructured Organometal Halide Perovskites, Science 338, 643-647, (2012). DOI: 10.1126/science.1228604

(24) Sadovniko, S.I., Ishchenko, A.V., and Weinstein, I.A., Synthesis and optical properties of nanostructured ZnS and heteronanostructures based on zinc and silver sulfides, J. Alloys and Comp. 831, 1548462 (2020). https://doi.org/10.1016/j.jallcom.2020.154846

(25) Yost, A.J., Ekanayaka, T. K. , Gurung, G. et al., *Influence of the Cation on the Surface Electronic Band Structure and Magnetic Properties of Mn:ZnS and Mn:CdS Quantum Dot Thin Films*, J. Phys. Chem. C 123, 24890−24898 (2019). https://doi.org/10.1021/acs.jpcc.9b06551

(26) Vinila, V., Jacob, R., Mony, A. , et al. *XRD Studies on Nano Crystalline Ceramic Superconductor PbSrCaCuO at Different Treating Temperatures.* Crystal Structure Theory and Applications, **3**, 1-9, (2014). doi: 10.4236/csta.2014.31001.

(27) Singh, R.K., Kumar, R., and Sing, J., Effect of precursors ratio on crystallinity and thermal stability of $CH_3NH_3PbI_3$, AIP Conference Proceedings 1832, 050056 (2017). https://doi.org/10.1063/1.4980289

(28) Whitfield, P.S., Herron, N., Guise, W.E. et al*., Structures, Phase Transitions and Tricritical Behavior of the Hybrid Perovskite Methyl Ammonium Lead Iodide,* Sci. Rep. **6,** 35685 (2016). https://doi.org/10.1038/srep35685

(29) Zhang, H. and Banfield, J.F., *Thermodynamic analysis of phase stability of nanocrystalline titania* J. Mater. Chem. 8(9), 2073–2076 (1998). DOI: https://doi.org/10.1039/A802619J

(30) Yost, A.J., Pimachev, A., Ho, C.C. et al., *Coexistence of Two Electronic Nano-Phases on a $CH_3NH_3PbI_{3-x}Cl_x$ Surface Observed in STM Measurements*, ACS Appl. Mater. Inter. 8, 29110−29116 (2016). https://doi.org/10.1021/acsami.6b07721

(31) Rimal, G., Pimachev, A., Yost, A.J., et al., *Giant photocurrent enhancement by transition metal doping in quantum dot sensitized solar cells*, Appl. Phys. Lett. 109, 103901 (2016). https://doi.org/10.1063/1.4962331

(32) Fox, M.A. *Optical Properties of Solids*, Vol. 3, Oxford University Press (2001).

(33) Gurung, G., Ekanayaka, T.K., Yost, A.J. and Paudel, T.R., *Absorption enhancement by transition metal doping in ZnS* Mater. Res. Express 6, 126550 (2019). https://doi.org/10.1088/2053-1591/ab56d6

(34) Patrycja Makuła, Michał Pacia, and Wojciech Macyk, *How to Correctly Determine the Band Gap Energy of Modified Semiconductor Photocatalysts Based on UV-Vis Spectra* J. Phys. Chem. Lett. *9* (23), 6814-6817 (2018). DOI: 10.1021/acs.jpclett.8b02892

(35) Dornelles, K., Roriz, M., Roriz, V.F., and Caram, R. *Thermal Performance of White Solar-Reflective Paints for Cool Roofs and the Influence on the Thermal Comfort and Building Energy use in Hot Climates* Conference: ISES Solar World Congress, Kassel, Germany (2011). DOI: 10.13140/RG.2.1.1745.5843

(36) Yang, J., Siempelkamp, B.D., Mosconi, E. et al., *Origin of the Thermal Instability in $CH_3NH_3PbI_3$ Thin Films Deposited on ZnO* Chem. Mater. 27, 4229−4236 (2015). https://doi.org/10.1021/acs.chemmater.5b01598

(37) Castro-Mendez, A.F., Hidalgo, J. and Correa-Baena, J.P., *The Role of Grain Boundaries in Perovskite Solar Cells* Adv. Energy Mater. 9, 1901489 (2019). https://doi.org/10.1002/aenm.201901489

(38) Jeng, J.Y., Chiang, Y.F., Lee, M.H., et al., *$CH_3NH_3PbI_3$ Perovskite/Fullerene Planar-Heterojunction Hybrid Solar Cells* Adv. Mater. 25, 3727 (2013). DOI:10.1002/adma.201301327

(39) You, J., Hong, Z., Yang, Y., et al. *Low-Temperature Solution-Processed Perovskite Solar Cells with High Efficiency and Flexibility* ACS Nano 8, 1674 (2014). https://doi.org/10.1021/nn406020d

(40) Li, C., Guerrero, A., Zhong, Y., and Huettner, S. *Origins and mechanisms of hysteresis in organometal halide perovskites* J. Phys.: Condens. Matter **29** 193001, (2017). DOI: 10.1088/1361-648X/aa626d

(41) Saidaminov, M.I., Haque, M.A., Almutlaq, J. et al., *Inorganic lead halide perovskite single crystals: phase-selective low-temperature growth, carrier transport properties, and self-powered photodetection* Adv. Opt. Mater. 5 1600704 (2017). https://doi.org/10.1002/adom.201600704

(42) Ilie, C.C., Guzman, F., Swanson, B.L., et al., *Inkjet printable-photoactive all inorganic perovskite films with long effective photocarrier lifetimes* J. Phys.: Condens. Matter 30, 18LT02 (2018). https://doi.org/10.1088/1361-648X/aab986